Heterogeneous & Homogeneous & Bio- & Nano-

CHEMCATCHEM

CATALYSIS

Accepted Article

Title: Probing the Influence of SSZ-13 Zeolite Pore Hierarchy in MTO Catalysis by NASCA microscopy and Positron Emission Profiling

Authors: Xiaochun Zhu, Nikolay Kosinov, Alexey Kubarev, Alexey Bolshakov, Brahim Mezari, Ivan Valastyan, Jan Philipp Hofmann, Maarten Roeffaers, Eva Sarakdi-Priboczki, and Emiel Hensen

To be cited as: *ChemCatChem* 10.1002/cctc.201700567

Link to VoR: http://dx.doi.org/10.1002/cctc.201700567

A Journal of ChemPubSoc Europe

WILEY-VCH

www.chemcatchem.org

ChemCatChem 10.1002/cctc.201700567

Probing the Influence of SSZ-13 Zeolite Pore Hierarchy in MTO Catalysis by NASCA microscopy and Positron Emission Profiling

Xiaochun Zhu, [a] [d] Nikolay Kosinov,[a] Alexey V. Kubarev,[b] Alexey Bolshakov,[a] Brahim Mezari,[a] Ivan Valastyan,[c] Jan P. Hofmann,[a] Maarten B. J. Roeffaers,[b] Eva Sarkadi-Pribóczki,[c] and Emiel J. M. Hensen,*[a]

Abstract: Understanding the role of the hierarchical pore architecture of SSZ-13 zeolites on catalytic performance in the Methanol-to-Olefins (MTO) reaction is crucial for guide the design of better catalysts. We investigated the influence of the space velocity on the performance of a microporous SSZ-13 zeolite, and several hierarchically structured SSZ-13 zeolites. Single catalytic turnovers, as recorded by Nanometer Accuracy by Stochastic Chemical reActions (NASCA) fluorescent microscopy verified that the hierarchical zeolites contain pores larger than the 0.38 nm apertures native to SSZ-13 zeolite. The amount of fluorescent events correlated well with the additional pore volume available due to hierarchical structuring of the zeolite. Positron Emission Tomography (PET) using 11C-labelled methanol was used to map the 2D spatial distribution of the deposits formed during the MTO reaction in the catalyst bed. PET imaging demonstrates that hierarchical structuring not only improves the utilization of the available microporous cages of SSZ-13 but also that the aromatic hydrocarbon pool species are involved in more turnovers before they condense into larger multi-ring structures that deactivate the catalyst.

Methanol is increasingly considered as an important chemical intermediate between coal and natural gas feedstock and olefinic building blocks extensively used in the chemical industry. Currently, the methanol-to-olefins (MTO) reaction is the most important in terms of installed capacity of all methanol-to-hydrocarbon reactions.[1,2,3,4]

A microporous silicoaluminophosphate material with the chabazite (CHA) framework topology (H-SAPO-34) is commercially the preferred catalyst.[5] One concern is the predicted scarcity of phosphorus, which is contained in typical silicoaluminophosphates up to 20 wt%.[6,7] The higher acidity of SSZ-13, the isostructural aluminosilicate analogue of H-SAPO-34, presents an opportunity to operate the MTO reaction at lower temperature and, in this way, to improve process economics.[8] On the other hand, the stronger acidity results in more rapid catalyst deactivation caused by multi-ring aromatics that block the pore system of the zeolite.[9] These multi-ring aromatics derive from fusion of aromatic hydrocarbon pool species, which are key reaction intermediates of the MTO reaction in small-pore zeolites.[10] Catalyst stability is impeded by the fact that these deposits form in the outer regions of the zeolite crystals and, accordingly, prevent access of methanol to internal regions. Introduction of mesopores within zeolite crystals is an elegant way to reduce these negative effects of diffusion limitations and improve the catalytic performance.[11,12,13] Common and scalable approaches such as steaming and alkaline leaching have a negative effect on MTO performance when applied to SSZ-13 zeolite.[14,15] Recently, in a series of papers we have demonstrated that, in a dual-template approach, specifically designed diquaternary ammonium surfactants $[C_{22}H_{45}\text{-}N^+(CH_3)_2\text{-}C_4H_8\text{-}N^+(CH_3)_2\text{-}C_4H_9]Br_2$ ($C_{22\text{-}4\text{-}4}\cdot Br_2$ for brevity) can limit SSZ-13 crystal growth, generating the desired mesoporosity.[16,17] A much cheaper alkylpiperidine surfactant has also been developed.[18] In another work, we showed that adding fluoride to the alkaline synthesis gel of SSZ-13 results in zeolite crystals with an additional system of micropores, slightly larger than the small eight membered-ring (8MR) apertures of the CHA framework.[19] Combined with diquaternary ammonium surfactant, this fluoride modification allows preparing trimodal porous SSZ-13 zeolite, which appears to be optimal in terms of total methanol conversion capacity.[20] In all of these cases, the additional porosity led to increased utilization of the CHA zeolite domains as evidenced by confocal fluorescence microscopy. However, there is no complete understanding of the benefit of the additional porosity on the catalytic performance in fixed-bed reactors. Moreover, the distribution of the additional micropores and mesopores over the zeolite crystal remains unclear. Recently, the need for advanced characterization of the texture of mesoporous zeolites has been stressed.[21,22,23] In the present study, we explore the relation between the spatial distribution of additional porosity in SSZ-13 zeolite crystals as probed by Nanometer Accuracy by Stochastic Chemical reActions (NASCA) microscopy and the deposition of coke in the catalyst bed by Positron Emission Tomography (PET).

For this purpose, we evaluated the catalytic MTO performance of a set of SSZ-13 zeolites with uni-, bi- and trimodal porosity. The investigated zeolites included (i) an SSZ-13 zeolite containing only micropores (SSZ-13-R), (ii) an SSZ-13 zeolite prepared in alkaline medium promoted by fluoride, which contains additional micropores slightly larger than the micropores of SSZ-13 (SSZ-13-F), and (iii) two trimodal porous SSZ-13 zeolites prepared with fluoride and using a diquaternary ammonium surfactant (in two different amounts) that generated additional mesoporosity (SSZ-13-F-M5 and SSZ-13-F-M25).[20] The most important physico-chemical properties of these zeolites are collected in Table 1. The significant textural differences are derived from Ar physisorption data (Fig. S1) and supported by

---

[a] X. Zhu, N. Kosinov, A. Bolshakov, B. Mezari, J.P. Hofmann, Prof. E.J.M. Hensen
Inorganic Materials Chemistry
Schuit Institute of Catalysis
Department of Chemical Engineering and Chemistry
Eindhoven University of Technology
P.O. Box 513, 5600 MB, Eindhoven, The Netherlands
E-mail: e.j.m.hensen@tue.nl
[b] A.V. Kubarev, M.B.J. Roeffaers,
Centre f or Surface Chemistry and Catalysis
Department of Microbial and Molecular Systems
KU Leuven
Kasteelpark Arenberg 23, 3001 Leuven, Belgium
[c] I. Valastyan, E. Sarkadi-Pribóczki
Cyclotron Applications
Institute for Nuclear Research
4026 Debrecen, Bemtér 18/c, Hungary
[d] X. Zhu
State Key Laboratory of Heavy Oil Processing
The Key Laboratory of Catalysis of CNPC
College of Chemical Engineering
China University of Petroleum
No. 18 Fuxue Road, Changping, Beijing 102249, China

X.Z. and N.K. contributed equally to this work.

Supporting information for this article is given via a link at the end of the document

SEM images (Fig. S2). High-resolution Ar physisorption demonstrated that the SSZ-13-F sample contains a small amount of micropores that are slightly larger than the CHA micropores.[19] All of these samples have similar Si/Al ratio with the predominant part of Al in the framework after calcination. The materials possess very similar acidic properties (both density and strength) as probed by ^{1}H MAS NMR (Table 1) and CO FTIR.[20]

Table 1. Chemical composition, Al speciation and textural properties of studied SSZ-13 catalysts.

Catalyst	Si/Al	Al$^{\cdot\cdot}$ (%)	Al$^{\cdot\cdot}$ (%)	BAS_{tot}	BAS_{acc}	S_L	S_{ext}	V_{tot}	V_{meso}	V_{micro}
SSZ-13-R	21	89	11	0.65	0.00	677	34	0.24	0.02	0.20
SSZ-13-F	22	88	12	0.67	n.d.	763	58	0.28	0.03	0.23
SSZ-13-F-M5	22	86	14	n.d.	n.d.	778	106	0.29	0.05	0.22
SSZ-13-F-M25	23	93	7	0.80	0.04	787	143	0.36	0.12	0.21

Si/Al – determined by ICP

Al^{IV}, Al^{VI} – relative amount of framework and extraframework Al (respectively) determined by ^{27}Al NMR

BAS_{tot} – total number of Brønsted acid sites (mmol/g) determined by ^{1}H MAS NMR

BAS_{acc} – Accessible Brønsted acid sites (mmol/g) as determined by IR of adsorbed pyridine

n.d. – not determined

S_L - Langmuir surface area (m^2/g) in the relative pressure range of 0.05–0.20

S_{ext} – external surface area (m^2/g) calculated by the t-plot method

V_{tot} - total pore volume (cm^3/g) at p/p_0= 0.97

V_{meso} - mesopore volume (cm^3/g) calculated by the BJH method

V_{micro} - micropore volume (cm^3/g) calculated by the t-plot method

The MTO performance of these zeolite catalysts was investigated at a temperature of 350 °C at different weight-hourly space velocities (WHSV, range 0.8 h^{-1} - 5.8 h^{-1}). The optimum reaction temperature for SSZ-13 zeolite in the MTO reaction is in the 350-375°C, much lower than the optimum temperature for SAPO-34.[8] Fig. 1 shows plots of methanol conversion *vs*. total amount of methanol converted to hydrocarbons for three different WHSV (details on conversion and selectivity in the Supporting Information as Fig. S3 and Tables S1-S3). All catalysts showed typical behavior: they could initially completely convert the methanol feed with ethylene and propylene as the main reaction products, but then quickly deactivated. For a given catalyst, the onset of deactivation occurred earlier when the WHSV was increased. The presence of additional pores larger than the native CHA micropores clearly led to increased methanol conversion capacity. This trend was evident at all applied space velocities. Fig. 2a depicts the total amount of converted methanol during one day on stream (TCC, total conversion capacity). For SSZ-13-R, TCC decreased as WHSV increased, which points to faster coke build-up when the feed rate of methanol was higher. We surmise that this is due to stronger diffusion limitations when the narrow micropores of SSZ-13-R become occupied with methanol and reaction products.[24] This result shows that a low WHSV is preferred for the reference zeolite. The hierarchical bi- and trimodal SSZ-13 zeolites displayed different behavior. The TCC was substantially higher than the reference zeolite and increased with increasing total pore volume. Moreover, an optimum in TCC was observed at intermediate WHSV for these three samples. Such optimum of the total methanol conversion capacity with respect to the methanol feed rate was also reported for other zeolite topologies such as MFI,[25] MOR,[26] BETA,[27] and SAPO-34.[28] Usually, this phenomenon is attributed to a trade-off between optimal rate of formation of hydrocarbon pool species[29] and diffusion limitations. Thus, hierarchical structuring of SSZ-13 increased the total amount of methanol the zeolite can convert before deactivation sets in.

Another factor critical to the commercial MTO process is the light olefins (ethylene, propylene) selectivity. It is well known that the pore topology of the zeolite has a pronounced effect on the product distribution. Some of the 8MR zeolites containing larger cages and small pore openings are preferred when light olefins are targeted.[30] Other factors that contribute to selectivity differences are the acidity,[31] the reaction conditions,[32] and the presence of coke,[33] and the use of co-reactants such as chloromethane.[34] We also investigated how the WHSV affected the product distribution. Fig. 2b depicts the $C_2^{=}/C_3^{=}$ ratio of the zeolites at a methanol conversion of 98 % as a function of WHSV. Strikingly, the substantial textural differences between the zeolites did not influence the $C_2^{=}/C_3^{=}$ ratio, that is to say that all zeolites displayed the same $C_2^{=}/C_3^{=}$ ratio at a particular WHSV (Fig. 2b). This indicates that for all studied catalysts the majority of catalytic events takes place inside the CHA pores, independent of the hierarchical structure, so that the mechanism of hydrocarbon formation is exactly the same. The $C_2^{=}/C_3^{=}$ ratio decreased from about 1.2 at the lowest WHSV to about 0.8 at the highest WHSV. A reasonable explanation for the increasing amount of propylene formed with increasing methanol feed rate is the higher degree of methylation of benzene intermediates, favoring formation of propylene, as shown by Song et al.[35]

Fig. 2c shows how the total light olefins (ethylene and propylene) selectivity depends on WHSV. For SSZ-13-R, the total light olefins selectivity is seen to decrease with increasing WHSV in a nearly linear fashion. The lower light olefins selectivity goes together with increasing contribution of C_4-C_6 products, *i.e.*, mainly C4 olefins and heavier paraffins and aromatics. There was less variation in the light olefins selectivity when the WHSV was increased from 0.8 h^{-1} to 2 h^{-1}. A further decrease of WHSV to 5.6 h^{-1} led to a significant loss of the light olefins selectivity, although not to the extent seen for SSZ-13-R. The light olefins selectivity correlates well with the additional porosity of hierarchical samples. We speculate that higher selectivity to the desired $C_2^{=}$ and $C_3^{=}$ products is due to lower intracrystalline residence time, which is the consequence of improved diffusion of reaction products in the extraframework pores.

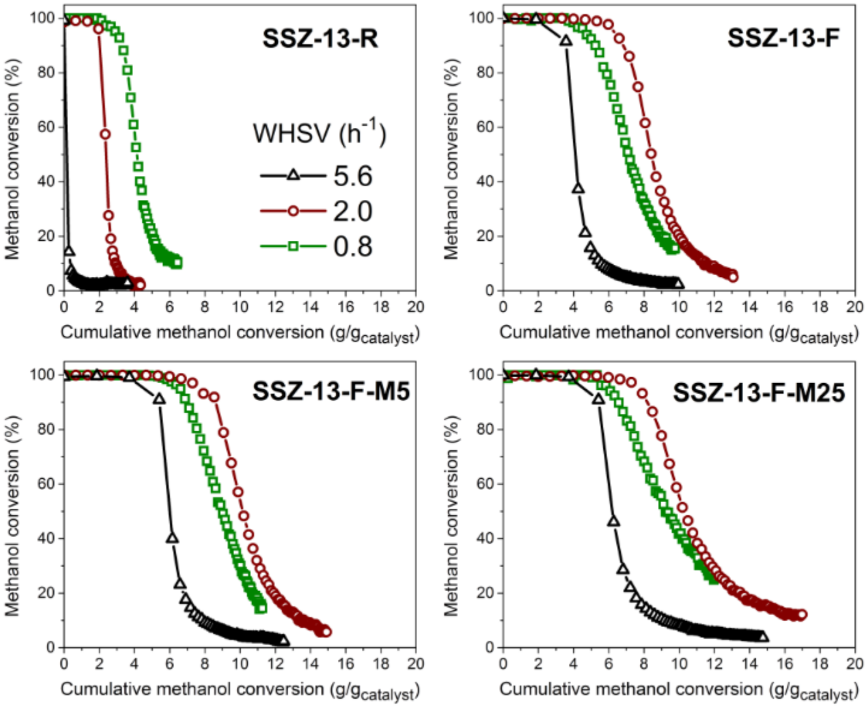

Figure 1. Methanol conversion as a function of the cumulative amount of converted methanol for different WHSV. Conditions: 350°C, 50 mg of catalyst, atmosphere pressure, 24 h.

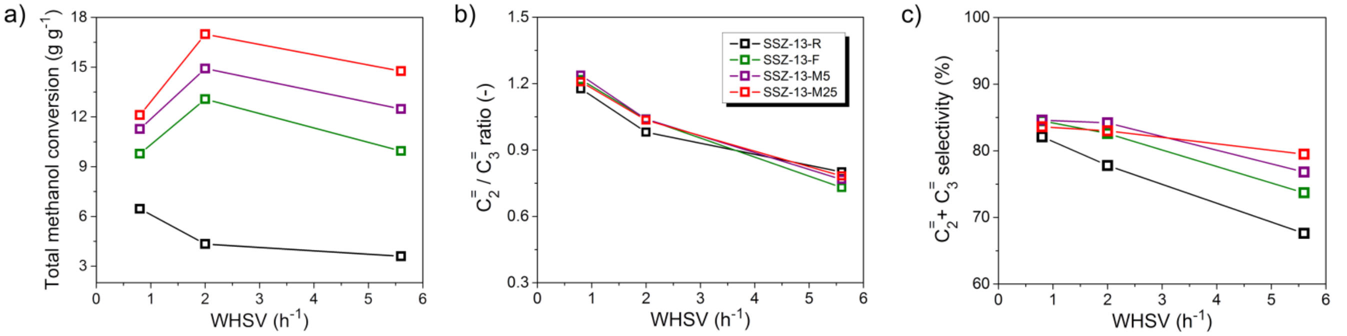

Figure 2. Influence of WHSV on the catalytic performance of the studied SSZ-13 catalysts: (a) total amount of methanol converted after 24 h time on stream, (b) ethylene/propylene ratio and (c) total ethylene + propylene selectivity at a methanol conversion of 98%.

The presence of additional extraframework porosity in the SSZ-13 zeolite particles was further investigated by super-resolution fluorescence NASCA microscopy.[36] This technique was already successfully applied to probe the spatial distribution of catalytic activity in MOR[37] and MFI[38,39] zeolites as well as in more complex materials like fluid catalytic cracking catalysts. [40] NASCA allows recording high-resolution reactivity maps of heterogeneous catalysts by following stochastic formation of fluorescent molecules.[41] In this work we applied acid-catalyzed oligomerization of furfuryl alcohol (FA) as a probe reaction (Figure 3) to highlight the spatial distribution of extraframework pores as the 0.5 nm kinetic diameter of FA is larger than the pore aperture of SSZ-13 zeolite (0.38 nm).

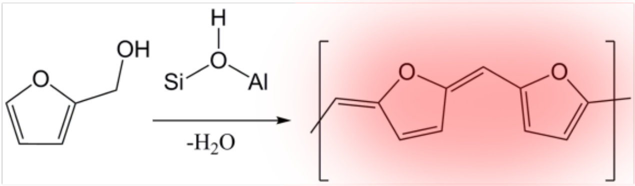

Figure 3. Acid-catalyzed oligomerization of FA yielding fluorescent products.

NASCA images were obtained by accumulation of the localized fluorescent emitters that appeared during the FA oligomerization in the middle plane of the zeolite crystals. For the SSZ-13-R reference sample, nearly no fluorescent events were observed in the zeolite crystal (Fig. 4e,I). This confirms that FA cannot enter the micropores of CHA and additionally suggests that the outer surface of the reference sample is devoid of acid sites, perhaps because of the presence of Si-enriched crust. On contrary, numerous reactions events were detected inside the particles of SSZ-13-F (Fig. 4f, j), SSZ-13-F-M5 (Fig. 4g, k) and SSZ-13-M25 (Fig. 4h, l). We infer that these events arise from reactions of FA at BAS located in the extraframework pores. Together with the textural data, these findings confirm that SSZ-13-F contains additional micropores, slightly larger than the pore apertures of CHA zeolite. Similar results were obtained for SSZ-13-F-M5 and SSz-13-F-M25. For the latter sample, the distribution of acid sites was less homogeneous than in the other two samples, this effect might be related to the very high concentration of mesoporogen applied for the synthesis of SSZ-13-F-M25, possibly leading to inhomogeneities and Al gradients within the crystals.

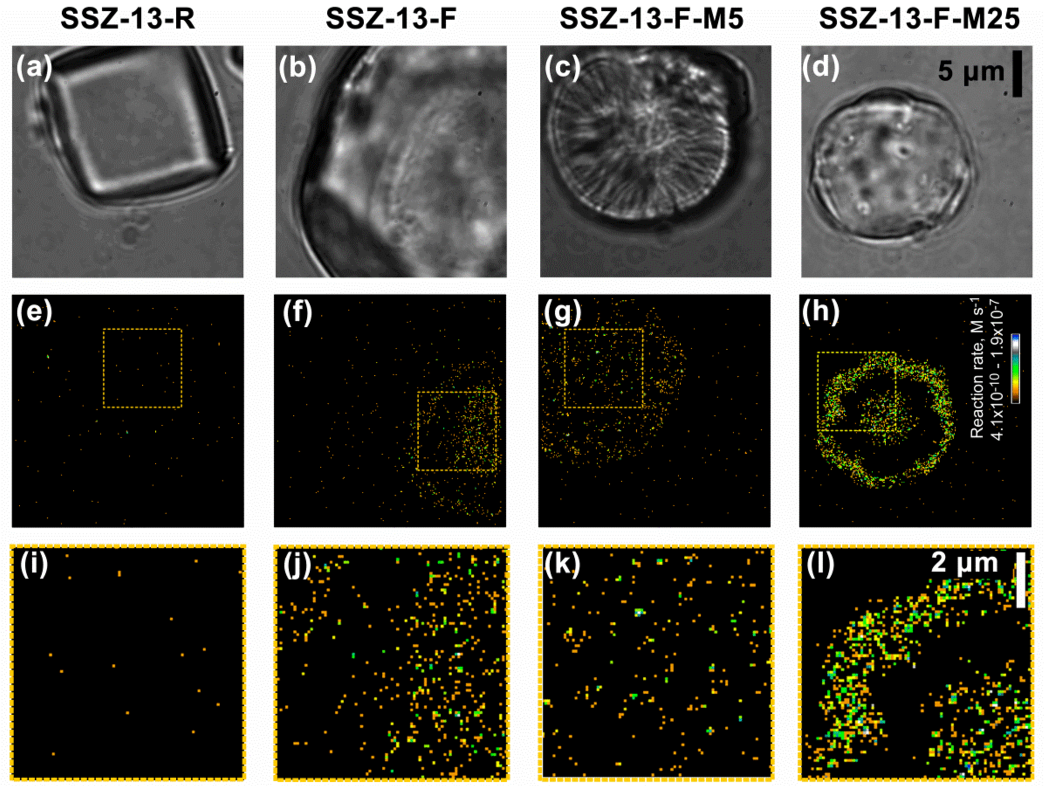

Figure 4. Bright-field optical transmission images of studied SSZ-13 samples (a) SSZ-13-R, (b) SSZ-13-F, (c) SSZ-13-F-M5, and (d) SSZ-13-F-M25; the corresponding NASCA reactivity maps and zoomed (x3) sections of furfuryl alcohol conversion on (e, i) SSZ-13-R, (f, j) SSZ-13-F, (g, k) SSZ-13-F-M5, and (h, l) SSZ-13-F-M25, obtained for 100 x 100 x 800 nm^3 voxels (*xyz*), reconstructed from 3000 frames (measurement time ≈ 150 s, false color scale shows the observed reaction rate in logarithmic scale).

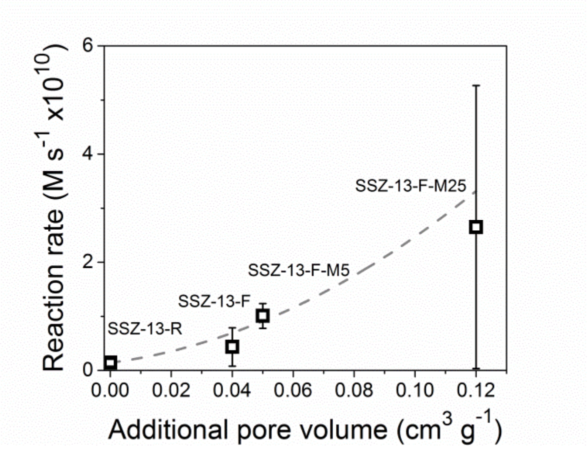

Figure 5. Averaged reaction rates (mol L^{-1} s^{-1}) independently observed for at least 4 different SSZ-13 crystals over 3000 frames (corrected to remove reappearing individual catalytic events) detected by NASCA analysis *vs.* the extraframework, non-CHA, pore volume derived from Ar physisorption**.**

Figure 5 shows the positive correlation between the total number of reaction events and the additional pore volume of the zeolite. Increased total pore volume leads to higher uptake of FA. Importantly, these data underpin the presence of additional extraframework pores throughout the zeolite particle, which will accelerate mass transfer during catalytic MTO reaction. The sample SSZ-13-F-M25 shows rather large deviation probably due to high loading of the mesoporogen. Nevertheless, with proper probe molecules, NASCA is a powerful tool for resolving the porosity distribution in hierarchical porous materials.

To better understand the influence of texture on the catalytic MTO performance, we employed positron emission tomography (PET) using ^{11}C as a label in methanol. This technique is based on the decay of ^{11}C (half time 20.334 min), which decays in ^{11}B and a positron. The positron annihilates with an electron, creating two γ-rays, which travel in opposite direction and can be detected by detectors allowing reconstruction of the position of the annihilation event.[42,43] The spatial resolution of this technique is limited to ca. 1 mm, the distance the positron can travel before annihilation. PET imaging using ^{11}C-labelled methanol allows monitoring the build-up of hydrocarbon pool species, which cannot leave the CHA pores and coke in the catalyst bed.[44] As catalysts were used SSZ-13-R and SSZ-13-F-M25 zeolites placed in a fixed-bed reactor. The feed was alternatingly switched between ^{12}C- and ^{11}C-labelled methanol. PET images were acquired at time intervals of 1 min. All images were corrected for the decay of ^{11}C and compressed as a function of time on stream (Figure 6, an original footage of the processes is provided in ESI). As a supplement to the PET images, the integrated radioactivity in each slice was plotted as function of time on stream. The colors in PET images correspond to the intensity of the emitted γ-rays.

The PET profile during the first 5 min of exposure of SSZ-13-R zeolites to ^{11}C-labelled methanol showed the build-up of carbon in a relatively narrow zone of the catalyst bed. This reaction zone became broader with time on stream. After the switch to normal methanol, the decay-corrected intensity only decreased slightly due to further reactions of part of the hydrocarbon pool species with non-labelled methanol. This result implies that most of the ^{11}C species remain in the same place. From the observation that the radioactivity only slightly decreases, we can conclude that the imaged species are mainly coke deposits that do not react further. The second 5 min exposure to ^{11}C-labelled methanol led to similar features in the PET images. From the observation that the radioactivity accumulated downstream of the first feature, we infer that upstream the catalyst bed has been fully deactivated. The reaction zone between the two features is also saturated by deactivated aromatics, which cannot be visualized by PET, as they are composed of ^{12}C atoms. Note that the given PET images for the second pulse have been obtained by subtracting the intensity from the first pulse. This explains why the radioactivity of the first pulse is not present in the images. A further striking difference is that the intensity of the second feature is much lower than that of the first one. Similar observations were made upon providing a third exposure to labelled methanol. The distance between the second and first feature is nearly the same as that between the third and second. This shows that the reaction zone in which carbon builds up in reaction intermediates moves at nearly constant pace through the catalyst bed. A fourth pulse did not lead to any detectable radioactive events, implying that the catalyst had completely deactivated. The lower intensity of the radioactive features as these move downstream the bed shows that less labelled methanol was involved in the formation if reaction intermediates. This must be due to pre-deposition of some intermediates in the cages of the zeolite. We speculate that these deposited intermediates must derive from secondary reactions of the olefins produced in the reaction zone downstream where methanol is completely converted.

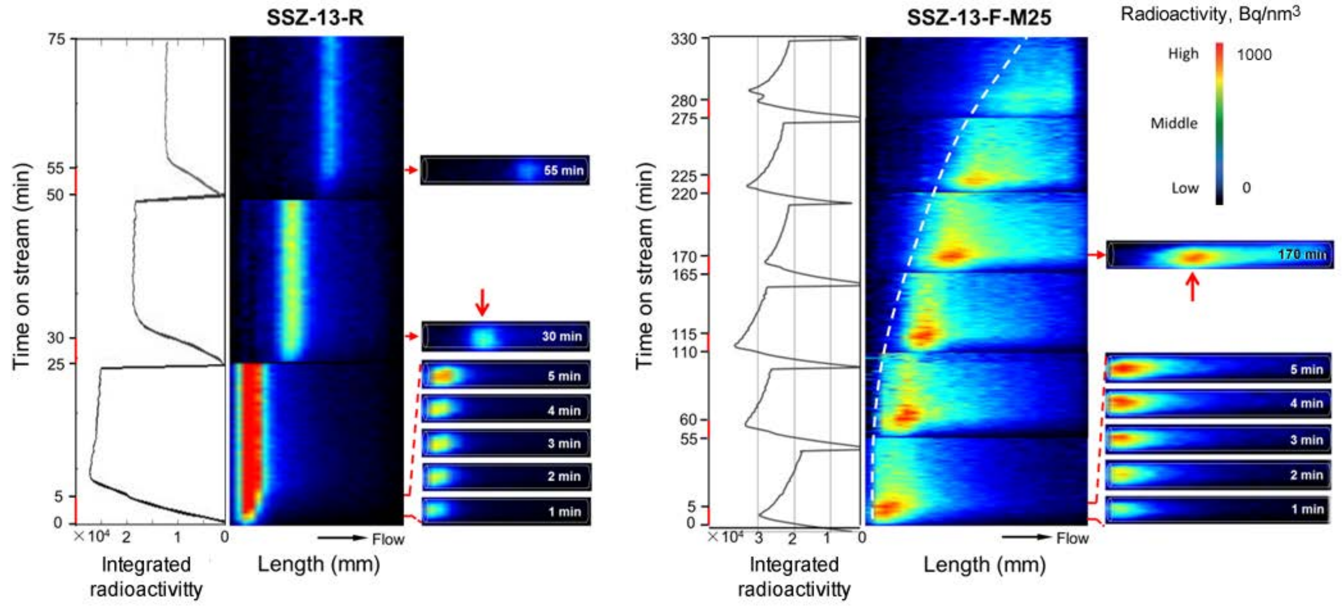

Figure 6. Positron emission tomography image series of (left) SSZ-13-R and (right) SSZ-13-F-M25 for ^{11}C-CH$_3$OH MTO reaction. Three ^{11}C methanol pulses were delivered to SSZ-13-R and six to SSZ-13-F-M25 (marked with red dashes). The radioactivity is decay-corrected in each slice along the catalyst bed (T = 350 °C; WHSV = 0.5 g g^{-1} h^{-1}).

The behavior of the hierarchical SSZ-13-F-M25 zeolite during a comparable PET experiment is different. After the initial build-up of deposited ^{11}C-containing species in a similar manner and in comparable amount as for SSZ-13-R, the decrease of the radioactivity is much stronger than for the reference zeolite. This implies that the aromatic hydrocarbon pool species were more actively involved in the MTO reaction cycle. This is also evident from the presence of ^{11}C atoms downstream of the hottest spot in the reactor. We attribute the longer involvement of the hydrocarbon pool species to the presence of additional pores that allow for better mass transport between the bulk gas phase and the micropore domains. Thus, whereas the micropores of SSZ-13-R became blocked by the aromatic pool species preventing access of methanol to the reaction intermediates, improved accessibility of methanol to these intermediates in hierarchically structured SSZ-13 results in reactions that decrease the ^{11}C content of the aromatic hydrocarbon pool species. Earlier, we have shown that a main reason for improved performance of the hierarchical zeolites is the more efficient utilization of the zeolite crystals in accommodating the hydrocarbon pool species. The present data also show that additional diffusion pathways in hierarchical SSZ-13 zeolite facilitate more turnover of the hydrocarbon pool. A tentative explanation is that faster mass transport maintains a high rate of methylation, preventing the formation of deactivating multi-ring aromatics.

Similar to SSZ-13-R, the reaction zone moves downstream the catalyst bed during subsequent exposures to labelled methanol. We used interval times of 50 min for these exposures. Nonetheless, the reaction zone in this case moves much slower through the catalyst bed than for SSZ-13-R. This demonstrates the much better utilization of the micropore space and the aromatic hydrocarbon pool species formed. In turn, the observation that the intensity did not decrease during consecutive exposures as it did for SSZ-13-R has likely to do with the much larger micropore space available for the MTO reaction, these phenomena are schematically illustrated by Fig. S4.

In conclusion, this study highlights the importance of additional intracrystalline porosity to effectively use SSZ-13 zeolite in the MTO reaction. These additional pores can be embedded by using a very cheap approach such as fluoride addition to SSZ-13 synthesis. NASCA microscopy demonstrates that such zeolite (SSZ-13-F) contains continuous pores with size larger than the CHA micropores. The performance of such zeolite can be further improved by introducing mesopores by using suitably designed surfactants. PET imaging demonstrates the very significant influence of the presence of additional pores: not only the available microporous cages of SSZ-13 are better utilized, also the aromatic hydrocarbon pool species are involved in more turnovers before they condense into larger multi-ring structures that deactivate the catalyst.

Experimental Section

Synthesis of mesoporogen $C_{22\text{-}4\text{-}4}\cdot Br_2$

1-bromodocosane (0.01 mol, Aldrich, 96 %) and N, N, N', N'-tetramethyl-1,4-butanediamine (0.06 mol, Aldrich, 98 %) were dissolved in ethanol (Biosolve, 99.9 %). The solution was refluxed in an oil bath at 70 °C for 12 h. After cooling to room temperature, the solution was cooled at 2 °C for several hours, then filtered and washed with diethyl ether. The resulting product $[C_{22}H_{45}\text{-}N^+(CH_3)_2\text{-}C_4H_8\text{-}N(CH_3)_2]Br$ was dried in a vacuum oven at 50 °C. 0.007 mol $[C_{22}H_{45}\text{-}N^+(CH_3)_2\text{-}C_4H_8\text{-}N(CH_3)_2]Br$ and 0.014 mol 1-bromobutane (Aldrich, 98 %) were dissolved in 110 ml of acetonitrile and stirred under reflux at 70 °C for 12 h. The resulting solution was cooled, filtered, washed with diethyl ether and dried in a vacuum oven at 50 °C. The product was $[C_{22}H_{45}\text{-}N^+(CH_3)_2\text{-}C_4H_8\text{-}N^+(CH_3)_2\text{-}C_4H_9]Br_2$, which will be further denoted as $C_{22\text{-}4\text{-}4}\cdot Br_2$.

Synthesis of zeolites

In a typical synthesis of H-SSZ-13, Ludox AS 40 (Aldrich, 40 wt%), aluminium hydroxide (Aldrich, reagent grade), sodium hydroxide (EMSURE, 50 wt%), N,N,N-trimethyl-1-adamantammonium hydroxide (TMAdaOH, SACHEM Inc. 25 wt%), and distilled water were mixed to obtain a gel with molar composition of 20 TMAdaOH : 7.5 Na_2O : 2.5 Al_2O_3 : 100 SiO_2 : 4400 H_2O. The resulting gel was stirred at room temperature for 2 h and then transferred into a 45 mL Teflon lined steel autoclave. The gel was crystallized statically at 160 °C for 6 days. The resulting reference zeolite is denoted as SSZ-13-R. Another SSZ-13 zeolite was synthesized by adding sodium fluoride (EMSURE, ≥ 99.5 %) to the above recipe of SSZ-13-R to give the following gel composition 20 TMAdaOH : 7.5 Na_2O : 10 NaF : 2.5 Al_2O_3 : 100 SiO_2 : 4400 H_2O. The final gel was crystallized statically at 160 °C for 10 days; the obtained zeolite is denoted as SSZ-13-F.

A set of mesoporous SSZ-13 zeolites, denoted as SSZ-13-F-Mx in which a fraction of TMAdaOH replaced by $C_{22\text{-}4\text{-}4}\cdot Br_2$ (x represents the fraction TMAdaOH replaced). The total N content of the synthesis gel was kept constant. $C_{22\text{-}4\text{-}4}\cdot Br_2$ was added to the gel for SSZ-13-F synthesis and the mixture was stirred for 2 h. The final gel was transferred into a Teflon-lined autoclave and crystallized statically at 160 °C for 12 days. After crystallization, the zeolite products were filtered, washed with distilled water and dried at 110 °C. The zeolites were calcined at 550 °C for 10 h under flowing air and ion-exchanged three times with 1.0 M NH4NO3 solutions followed by calcination at 550 °C for 4 h in order to obtain their proton forms.

Catalytic activity measurements

The zeolite samples were pressed into wafers, which were then crushed and sieved to obtain particles in the range 250−500 µm. Catalytic activity measurements were carried out in a quartz tubular fixed-bed reactor with 50 mg catalyst loading. The inner diameter of the quartz tube reactor is 4 mm. Prior to reaction, the catalyst was pretreated at 550 °C in synthetic air (30 ml min^{-1}) for 1 h. The MTO reaction was performed at 350 °C. Methanol (Merck, 99 %) was introduced to the reactor by leading a flow of 30 ml min^{-1} of He through a saturator kept at −17.2 °C. The resulting WHSV is 0.8 g g^{-1} h^{-1}. For the purpose of investigating the influence of different WHSV on the performance of zeolite catalysts, the temperature of saturator was changed to −2 °C and 17 °C to obtain the WHSV of 2 and 5.6 g g^{-1} h^{-1}, respectively. The product effluent was analysed by online gas chromatography (Compact GC Interscience equipped with TCD and FID detectors with RT-Q-Bond and Al_2O_3/KCl columns, respectively). The reaction was followed for 24 h time on stream. Methanol conversion is based on the inlet and outlet concentrations of methanol as determined by GC analysis of the reactor feed before and after the reaction and the reactor effluent during reaction. Dimethylether was considered as a reactant in the calculation of the conversion and selectivity.

NASCA microscopy

For the microscopy experiments, crystals were deposited on a cover glass through spin-coating from an aqueous suspension. Then the samples were calcined in three stages: (1) heating to 80°C (1°C/min) and drying at this temperature for 1 h in order to remove easily desorbing molecules; (2) heating to 120°C (1°C/min) and drying at this temperature for 1 h to remove physisorbed water and (3) heating to 450°C (1°C/min) and prolonged calcination at this temperature for 50 h to remove fluorescent contaminants. After cooling down the samples were immediately used in microscopy experiments to prevent re-adsorption of fluorescent contaminants. Liquid phase experiments on an inverted epi-fluorescence microscope were performed using a PTFE container sealed to the glass cover slip via a silicone rubber gasket. Furfuryl alcohol (Aldrich) oligomerization was used as a fluorogenic reaction, for that aqueous solution (6.7 wt.%) of furfuryl alcohol was added to the sample and allowed to react for 1-2 h. For every sample 4-5 different crystals were independently measured. The NASCA investigation was conducted on a wide-field setup based on an inverted microscope IX71 (Olympus) platform equipped with an oil immersion objective lens (100X, 1.4 NA, Olympus) and a Diode-Pumped Solid State Excelsior laser (Spectra-Physics). The latter provided a laser excitation with λ = 532 nm of ≈ 100 W/cm^2 power on the sample. Fluorescence imaging (545 nm long pass filter) was performed using an ImagEM Enhanced C9100-13 EM-CCD camera (Hamamatsu). Further single molecule identification, localization and generation of NASCA images were performed using an in-house developed set of open-source plugin routines(https://bitbucket.org/pdedecker/localizer) [45] for IgorPro v.6.34A software (Wavemetrics). The presented NASCA images were obtained by the accumulation of localized fluorescent emitters which appeared during reaction in the focal plane in the middle of the crystals.

Positron emission tomography

The small PET scanner, which has a spatial resolution of ~ 1.3 mm and consists of 12 detector modules (one module has 35 × 35 scintillation crystals in an array configuration) in a full ring configuration, was used in this study to image the location and quantitative distribution of ^{11}C-containing species along the catalyst bed during the MTO reaction. Two 511 keV gamma photons originating from positron annihilation of a radioisotope were used to provide a more accurate mapping. PET images were collected within a time interval of 1 min. The images were further processed by using decay correction and normalization.[46] Contour-based attenuation correction was also applied on the data. For the MTO reaction, 300 mg of SSZ-13 zeolites were loaded into a quartz reactor with inner diameter of 4.5 mm. The catalyst was firstly dehydrated at 550 °C in 30 ml min^{-1} He flow with a rate of 10 °C min^{-1} and kept for 1 h. Then the temperature was lowered to 350 °C and ^{11}C-labeled methanol and nonradioactive methanol were intermittently introduced to the reactor (i.e., feeding of ^{11}C-labeled methanol for 5 min first for all samples and then nonradioactive methanol for 20 min for SSZ-13-R and 50 min for SSZ-13-F-M25) by leading a flow of 10 ml min^{-1} He through liquid methanol kept at room temperature. The products of MTO reaction were analyzed by radio-GC with a PLOT-Q column. A flame ionization detector (FID) and a radioactivity detector (RD) were applied to detect all the compounds and ^{11}C-labeled species, respectively.

Acknowledgements

The authors acknowledge financial support from the Technology Foundation (STW) of the Netherlands Organization for Scientific Research (NWO) and the China Scholarship Council. M.B.J.R. thanks the “Fonds voor Wetenschappelijk Onderzoek”(Grant G0962.13), the KU Leuven Research Fund (OT/12/059) and the European Research Council (ERC, Starting Grant LIGHT 307523).

Keywords: hierarchical zeolite • SSZ-13 • single molecule fluorescence • PET • methanol-to-olefins

GRAPHICAL ABSTRACT

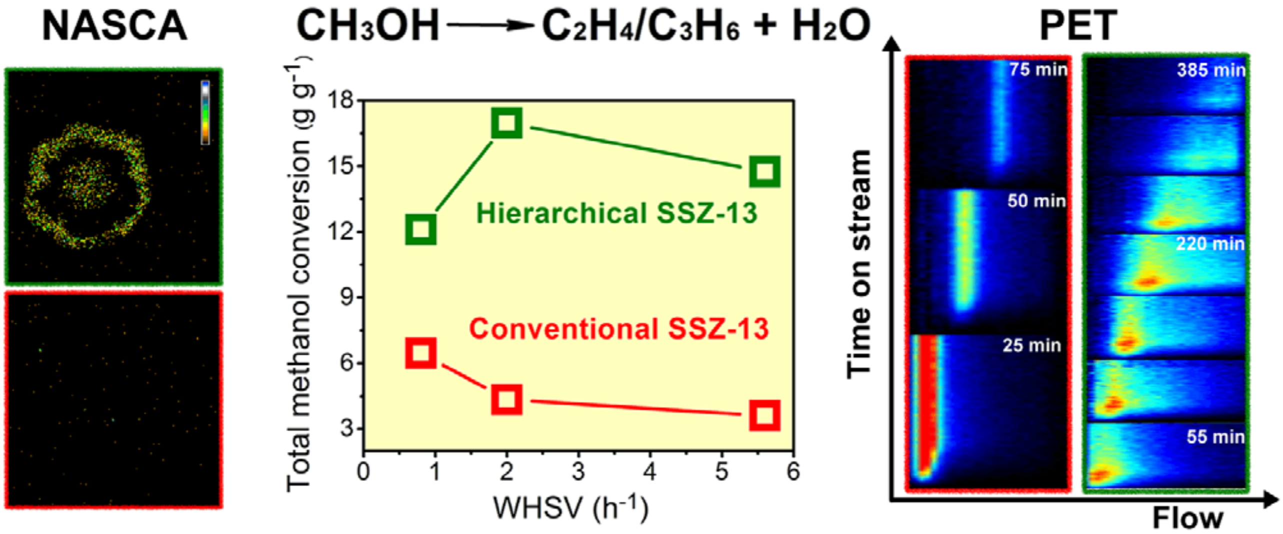

REFERENCES

1. Hickman, D. A.; Schmidt, L. D. *Science* **1993**, *259*, 343−346.
2. Asadullah, M.; Ito, S.; Kunimori, K.; Yamada, M.; Tomishige, K. *J. Catal*. **2002**, *208*, 255−259.
3. Haw, J. F.; Song, W.; Marcus, D. M.; Nicholas, J. B. *Acc. Chem. Res*. **2003**, *36*, 317−326.
4. Wang, W.; Hunger, M. *Acc. Chem. Res*. **2008**, *41*, 895−904.
5. Xu, S.; Zheng, A.; Wei, Y.; Chen, J.; Li, J.; Chu, Y.; Zhang, M.; Wang, Q.; Zhou, Y.; Wang, J.; Deng, F.; Liu, Z. *Angew. Chem*. **2013**, *125*, 11778−11782.
6. Gilbert, N. *Nature* **2009**, *461*, 716–718.
7. Cordell, D.; Rosemarin, A.; Schroder, J. J.; Smit, A. L. *Chemosphere* **2011**, *84*, 747–758.
8. Bleken, F.; Bjørgen, M.; Palumbo, L.; Bordiga, S.; Svelle, S.; Lillerud, K. P.; Olsbye, U. *Top. Catal*. **2009**, *52*, 218−228.
9. Borodina, E.; Meirer, F.; Lezcano-González, I.; Mokhtar, M.; Asiri, A. M.; Al-Thabaiti, S. A.; Basahel, S. N.; Ruiz-Martinez, J.; Weckhuysen, B. M. *ACS Catal.* **2015**, *5* (2), 992–1003.
10. Erichsen, M.W.; Morten, M.; Svelle, S.; Sekiguchi, O.; Uggerud, E.; Olsbye, U. ChemCatChem **2015**, *7*, 4143-4147.
11. Bjørgen, M.; Joensen, F.; Holm, M. S.; Olsbye, U.; Lillerud, K. P.; Svelle S. *Appl. Catal. A, Gen*. **2008**, *345*, 43−50.
12. Kim, J.; Choi, M.; Ryoo, R. *J. Catal*. **2010**, *269*, 219−228.
13. Milina, M.; Mitchell, S.; Crivelli, P.; Cooke, D.; Pérez-Ramírez, J. *Nat. Commun*. **2014**, *5*, 3922−3931.
14. Sommer, L.; Mores, D.; Svelle, S.; Stöcker, M.; Weckhuysen, B. M.; Olsbye, U. *Microporous Mesoporous Mater*. **2010**, *132*, 384−394.
15. Aramburo, L. R.; Ruiz-Martínez, J.; Sommer, L.; Arstad, B.; Buitrago-Sierra, R.; Sepúlveda-Escribano, A.; Zandbergen, H. W.; Olsbye, U.; de Groot, F. M. F.; Weckhuysen, B. M. *ChemCatChem* **2013**, *5*, 1386−1394.
16. Wu, L.; Degirmenci, V.; Magusin, P. C. M. M.; Szyja, B. M.; Hensen, E. J. M. *Chem. Commun*. **2012**, *48*, 9492−9494.
17. Wu, L.; Degirmenci, V.; Magusin, P. C. M. M.; Lousberg, N. J. H. G. M.; Hensen, E. J. M. *J. Catal*. **2013**, *298*, 27−40.
18. Zhu, X.; Rohling, R.; Filonenko, G.; Mezari, B.; Hofmann, J. P.; Asahina, S.; Hensen, E. J. M. *Chem. Commun*. **2014**, *50*, 14658−14661.
19. Zhu, X.; Kosinov, N.; Hofmann, J. P.; Mezari, B.; Qian, Q.; Rohling, R.; Weckhuysen, B. M.; Ruiz-Martínez, J.; Hensen, E. J. M. *Chem. Commun.* **2016**, *52* (15), 3227–3230.
20. Zhu, X.; Hofmann, J. P.; Mezari, B.; Kosinov, N.; Wu, L.; Qian, Q.; Weckhuysen, B. M.; Asahina, S.; Ruiz-Martínez, J.; Hensen, E. J. M. *ACS Catal*. **2016**, *6*, 2163−2177.
21. Mitchell, S.; Pinar, A. B.; Kenvin, J.; Crivelli, P.; Kärger, J.; Pérez-Ramírez, J. *Nat. Commun*. **2015**, *6*, 8633−8646.
22. Wei, Y.; Parmentier, T. E.; de Jong, K. P.; Zečević, J. *Chem. Soc. Rev*. **2015**, *44*, 7234−7261.
23. Kenvin, J.; Mitchell, S.; Sterling, M.; Warringham, R.; Keller, T. C.; Crivelli, P.; Jagiello, J.; Pérez-Ramírez, J. *Adv. Funct. Mater.* **2016**, *26*, 5621−5630.
24. Guisnet, M; Costa, L.; Ribeiro, F. R. *J. Mol. Catal. A Chem.* **2009**, *305*, 69–83.
25. Chang, C. D.; Silvestri, A. J. *J. Catal.* **1997,** *47,* 249–259.
26. Marchi, A. J.; Froment, G. F. *Appl. Catal. A, Gen.* **1993**, *94*, 91–106.
27. Bjorgen, M.; Kolboe, S. *Appl. Catal. A Gen.* **2002**, *225*, 285–290.
28. Wu, X.; Abraha, M. G.; Anthony, R. G. *Appl. Catal. A Gen.* **2004**, *260*, 63–69.
29. Haw, J. F. ; Song, W.; Marcus, D. M.; Nicholas, J. B. *Acc. Chem. Res.* **2003**, *36*, 317–326..
30. Olsbye, U.; Svelle, S.; Bjørgen, M.; Beato, P.; Janssens, T. V. W.; Joensen, F.; Bordiga, S.; Lillerud, K. P. *Angew. Chem. Int. Ed*. **2012**, *51*, 5810−5831.
31. Wilson, S.; Barger, P. *Microporous Mesoporous Mater*. **1999**, *29*, 117−126.
32. Tian, P.; Wei, Y.; Ye, M.; Liu, Z. *ACS Catal*. **2015**, *5*, 1922−1938.
33. Chen, D.; Rebo, H. P.; Moljord, K.; Holmen, A. *Ind. Eng. Chem. Res*. **1997**, *36*, 3473−3479.
34. Li, J.; Qi, Y.; Liu, Z.; Liu, G.; Zhang, D. *Catal. Lett*. **2008**, *121*, 303−310.
35. Song, W.; Fu, H.; Haw, J. F. *J. Am. Chem. Soc.* **2001**, *123*, 4749–4754.
36. Roeffaers, M. B. J.; De Cremer, G.; Libeert, J.; Ameloot, R.; Dedecker, P.; Bons, A.-J.; Buckins, M.; Maartens, J. A.; Sels, B. F.; De Vos, D. E.; Hofkens, J. *Angew. Chem. Int. Ed*. **2009**, *48*, 9285−9289.
37. Liu, K.-L.; Kubarev, A. V.; Van Loon, J.; Uji-i, H.; De Vos, D. E.; Hofkens, J.; Roeffaers, M. B. J. *ACS Nano*. **2014**, *8*, 12650−12659.
38. Ristanović, Z.; Hofmann, J. P.; De Cremer, G.; Kubarev, A. V.; Rohnke, M.; Meirer, F.; Hofkens, J.; Roeffaers, M. B. J.; Weckhuysen, B. M. *J. Am. Chem. Soc.* **2015**, *137* (20), 6559–6568.
39. Ristanović, Z.; Kubarev, A. V.; Hofkens, J.; Roeffaers, M. B. J.; Weckhuysen, B. M. *J. Am. Chem. Soc.* **2016**, *138*, 13586–13596.
40. Ristanović, Z.; Kerssens, M. M.; Hendriks, F. C.; Dedecker, P.; Hofkens, J.; Roeffaers, M. B. J.; Weckhuysen, B. M. *Angew. Chemie Int. Ed.* **2015**, *54*, 1836–1840.
41. Roeffaers, M. B. J.; Sels, B. F.; Uji-I, H.; De Schryver, F. C.; Jacobs, P. A.; De Vos, D. E.; Hofkens, J. *Nature* **2006**, *439*, 572–575.
42. de Jong, A. M.; Hensen E. J. M.; van Santen, R. A. ‘Positron Emission Tomography and Profiling’ in ‘In-Situ Spectroscopy of Catalysts’ in B.M. Weckhuysen (Ed.) pp. 271−292, American Scientific Publishers, California, 2004.
43. van Santen, R. A.; Anderson, B. G.; Cunningham, R. H.; Mangnus, A. V. G.; van Ijzendoorn, L.; de Voigt, M. J. A. *Angew. Chemie Int. Ed*. **1996**, *35*, 2785–2787.
44. Sarkadi-Pribóczki, E.; Valastyan, I.; Molnar, J. *ChemPlusChem* **2013**, *78*, 830−836.
45. Dedecker, P.; Duwé, S.; Neely, R. K.; Zhang, J.; *J. Biomed. Opt*. **2012**, *17*, 126008..
46. van Santen, R. A.; Anderson, B. G.; Cunningham, R. H.; Mangnus, A. V. G.; van Ijzendoorn, L.; de Voigt, M. J. A. *Angew. Chemie Int. Ed*. **1996**, *35*, 2785–2787.